Optical ferromagnetic resonance studies of thin film magnetic structures

R J Hicken, A Barman, V V Kruglyak and S Ladak

School of Physics, University of Exeter, Stocker Road, Exeter EX4 4QL, UK

Abstract

We have used a magneto-optical pump-probe technique to stimulate and characterize small amplitude precession of the magnetization in a variety of thin film magnetic structures. The sample is stimulated by an optically triggered magnetic field pulse and its response probed by means of a stroboscopic measurement of the magneto-optical Kerr effect. We demonstrate that the experimental technique is sensitive to small amplitude deflections of the magnetization and present formulae that describe the frequency of precession in continuous films containing either one or two magnetic layers. We show how the dependence of the precession frequency upon the orientation and magnitude of the static field may be used to characterize a 100 Å Co thin film, a $Ni_{81}Fe_{19}(50 Å)/Cu(20 Å)/Co(50 Å)/IrMn(100 Å)$ spin-valve structure, and a square $Ni_{81}Fe_{19}$ element of 10 μm side and 150 nm thickness. Information may be obtained about the g factor, demagnetizing field, exchange bias effect and magnetic anisotropy within an individual ferromagnetic layer, and about the coupling between layers. We deduce the presence of a four-fold anisotropy in the square element that is associated with non-uniformity of the magnetization. Time resolved images show that the dynamic magnetization is generally non-uniform. A stripe pattern is observed when the static field is significantly larger than the anisotropy field. Measurements at low field show that the dynamic magnetization initially has a regular pattern associated with the underlying domain structure, but then evolves into a highly disordered state. Finally we discuss the outlook for further development and application of the experimental technique.

1. Introduction

Thin film magnetic materials have been the subject of intense study for a number of decades. The stabilization of new structural phases and modulation of chemical composition at the nanoscale have led to new magnetic properties of significant technological interest. These new materials support a spectrum of GigaHertz frequency magnetic excitations that have been studied by techniques such as ferromagnetic resonance (FMR) in microwave cavities, and Brillouin light scattering (BLS) [1]. Careful studies of the variation of the excitation frequency have been made to quantify magnetic properties such as anisotropy and exchange coupling.

Thin film magnetic materials find immediate application within the magnetic data storage industry although other opportunities exist for the use of thin film magnetic materials within communications technology. For example, fast magneto-optical devices are of interest for optical telecommunications, while the resonant absorption of microwaves by magnetic material can be utilized in wireless applications. Within a magnetic hard disk drive, thin film magnetic materials form the basis of both the storage medium and the read and write transducers. While the storage medium consists of a single layer of nanoscale grains, the transducers are assembled from lithographically defined thin film elements of nanometre thickness. Future storage formats are also likely to include the magnetic random access memory (MRAM) chip that contains an array of matrix-addressed sub-micron magnetic elements. The continuing need to store larger amounts of data has led first to the reduction of bit and transducer sizes, and second to increased record and replay rates.

Further technological development requires the picosecond magnetization dynamics of thin film elements with micron

and nanometre dimensions to be understood. Many transient processes, such as magnetic switching, require precise control of the relative phase of different frequency components that may also interact due to the inherent non-linearity of the magnetization dynamics. These processes are most conveniently studied in the time domain and so an alternative is sought to conventional FMR and BLS, which are essentially frequency domain techniques. Measurements must also be made with very high spatial resolution, which favours the use of a focused optical probe.

Recently the magneto-optical pump probe technique has emerged as a new means by which to study femto and picosecond magnetization dynamics. The pump and probe are derived from the same single laser pulse so that the time delay between their arrival at the sample is determined only by their respective path lengths. The probe pulse is used to determine the instantaneous magnetic state of the sample, and so, by varying the time delay, the evolution of the magnetic state after excitation by the pump pulse may be mapped out with a time resolution that is limited only by the laser pulse width. Within the basic measurement procedure there is considerable flexibility to change the nature of the pump and probe. The technique has been applied to semiconductor materials where a circularly polarized pump may be used to create a transient magnetization through the process of optical orientation [2]. Alternatively the pump pulse may be used to heat a magnetic sample and cause it to demagnetize [3, 4]. A reorientation of the magnetization may be achieved by changing the total effective magnetic field that acts upon the sample. For example, heating by the pump pulse can lead to a significant modification of an anisotropy [5, 6] or exchange bias [7] field while leaving the spontaneous magnetization almost unchanged. More generally an external pulsed magnetic field can couple to any magnetic sample. Pulsed magnetic fields have been generated either directly with photoconductive switches [8] and photodiodes [9, 10] or with optically triggered electronic pulse generators [10], albeit with the introduction of additional trigger jitter. Similar freedom exists in the choice of the probe process. The linear magneto-optical Kerr effect (MOKE) is sensitive to all three components of the vector magnetization [11], while magnetic second harmonic generation (MSHG) has proved to be effective in studying the evolution of the in-plane magnetization components [10]. Alternatively, time resolved photoluminescence [12] and two-photon photoemission [13] have been used to study spin relaxation and spin dependent electronic relaxation.

Since the first measurements on EuS [8], the field pumped technique has been applied to an increasingly wide variety of materials, including Fe [14], Co [15], $Fe_{1-x}Co_x$ [9] and $Ni_{81}Fe_{19}$ [16]. The latter material has attracted particular attention due to its use in recording head transducers and because its small in-plane anisotropy and damping favour the excitation of a long-lived precessional motion. Small amplitude precessional oscillations have been studied in order to characterize magnetic anisotropy and damping [17], and also to demonstrate coherent control of magnetization precession [18, 19]. The spatial uniformity of the precession has begun to be explored [15, 16] leading to a realization that long wavelength magnetostatic modes play an important

role in experiments in which either the pulsed field is inhomogeneous [20, 21] or the lateral dimensions of the sample are small [22, 23]. Finally, large amplitude reorientation of the magnetization has been studied, both on nanosecond timescales [24] where domain wall propagation is significant, and on picosecond timescales where precessional motion dominates [10, 25, 26].

In this paper we show how the magneto-optical pump-probe technique can be used to perform optical FMR measurements upon single and multilayered magnetic films and also microscale thin film elements. We restrict ourselves to the magnetic field pumped technique in which a small amplitude precession is induced while leaving the magnitude of the spontaneous magnetization unchanged. We show that this technique may be used to obtain much of the information previously obtained from microwave FMR and BLS measurements. Finally we show how time resolved magnetic imaging may be used to study the coherence of precessional dynamics and provide unique information about ultrafast micromagnetic behaviour.

2. Experimental apparatus

The experimental apparatus required to make field-pumped measurements is shown in schematic form in figure 1 and has been described in detail elsewhere [27]. The Ti : sapphire laser supplies 100 fs pulses at a repetition rate of 82 MHz. All measurements described in this paper were performed at a wavelength close to 790 nm. These pulses are divided into two parts with the pump beam being passed through an optical delay line in order to control its time of arrival at the structure shown in figure 2. This structure consists of an interdigitated photoconductive switch connected to a coplanar strip transmission line on which the sample is overlaid. Initially samples were grown on transparent substrates so that the sample response could be probed through the sample substrate. However, by fabricating the transmission line
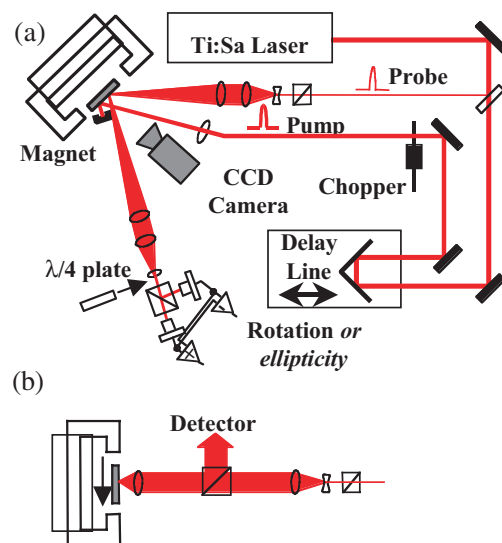

Figure 1. (*a*) The pump-probe apparatus is shown in schematic form for the case that the probe is focused with a long focal length lens. (*b*) The optical geometry is shown when a microscope is used to focus the probe.
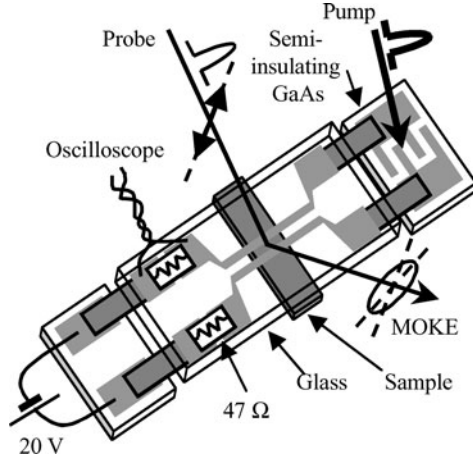
Figure 2. The photoconductive switch and transmission line structure used to deliver the pulsed magnetic field to the sample is shown in schematic form.

on a transparent substrate, measurements can be made on any sample by instead probing through the transmission line substrate. Faraday rotation from the glass substrate could in principle contribute to the measured magneto-optical signal. However, this contribution is expected to be small and in practice is not observed. Gating the photoconductive switch with the pump pulse causes a current pulse to propagate along the transmission line, where the associated magnetic field stimulates the sample, before being absorbed in the terminating surface mount resistors. The width of the transmission line tracks is typically reduced to less than $100\,\mu$m so that pulsed fields greater than 1 Oe may be generated. The pump beam is focused with a single lens to a spot size greater than $100\,\mu$m that spans many fingers of the switch. This ensures that the magnitude of the field pulse is unchanged when a piezoelectric stage is used to scan the entire sample structure relative to the fixed pump and probe beams. The amplitude of the pulsed field can be calculated from the amplitude of the current pulse, which may be estimated by monitoring the voltage drop across one of the terminating resistors.

A small probe spot is required to properly explore the homogeneity of the magnetization dynamics. The probe beam is first expanded in order to reduce the beam divergence. Thereafter two different optical configurations have been used. First the probe beam has been focused to a diameter of about $15\,\mu$m using an achromatic doublet with a focal length of $16\,$cm. Second a microscope objective has been used to achieve a sub-micron spot at normal incidence. The reflected probe beam is then picked off with a beam splitter cube placed in the path of the expanded beam. While the second configuration obviously provides better spatial resolution, the first approach is sometimes advantageous. The angle of incidence of the probe is well defined, so the magneto-optical response may be more easily related to the instantaneous orientation of the magnetization vector, and the signal to noise ratio can be better. Using the full beam from the microscope objective, there is no net contribution from the longitudinal Kerr effect and the out of plane component of the magnetization is sensed by means of the polar Kerr effect. In both configurations described above the change in polarization of the reflected probe beam is analysed by means of an optical

bridge. By chopping the pump beam, phase sensitive detection allows changes in rotation and ellipticity angle of down to $1\,\mu$deg to be resolved.

3. Theory of spin excitations

The response of the magnetization of a thin film magnetic element to a pulsed field may be described by the Landau–Lifshitz–Gilbert equation

$$\frac{\partial \boldsymbol{M}}{\partial t} = -|\gamma| \boldsymbol{M} \times \boldsymbol{H}_{\text{eff}} + \frac{\alpha}{M}\left(\boldsymbol{M} \times \frac{\partial \boldsymbol{M}}{\partial t}\right), \tag{1}$$

in which $\boldsymbol{M}$, $\boldsymbol{H}_{\text{eff}}$, $\gamma = g\mu_{\text{B}}/\hbar$, and α are the magnetization, the total effective field acting upon the magnetization, the magnetomechanical ratio, and the Gilbert damping constant, respectively. Although this equation must in general be solved numerically by means of finite element methods, other solutions may be obtained when certain simplifying assumptions are made. Assuming that the static magnetization is uniform, a variety of excitations with finite wave vector are possible [28] but these will not be considered further here. If the dynamic magnetization is assumed to be uniform (a zero wave vector excitation) then even large amplitude displacements of the magnetization may be described by a single pair of coupled differential equations that may be easily solved numerically [29]. Having obtained the trajectory of the magnetization, it is in principle straightforward to calculate the expected magneto-optical signal for a particular measurement configuration using generalized reflection coefficients that contain all three components of the vector magnetization [14]. This procedure becomes more complicated when the angle of incidence and the orientation of the plane of incidence vary through a large range, as when a microscope objective is used to focus the probe beam.

In the limit of small amplitude motion, algebraic expressions for the frequencies of the various resonant modes of multilayered elements may be obtained. We demonstrate this by considering a continuous sheet of material that contains two magnetic layers separated by a non-magnetic layer. Neglecting the damping term we obtain

$$\frac{\partial \boldsymbol{M}_i}{\partial t} = -|\gamma_i|\,[\boldsymbol{M}_i \times \boldsymbol{H}_{\text{eff}_i}], \tag{2}$$

where the index $i = 1, 2$ denotes the magnetic layer under consideration. The total effective magnetic field acting upon layer i may be written as

$$\boldsymbol{H}_{\text{eff}_i} = -\frac{1}{M_i}\nabla_{u_i} E_{\text{eff}_i}, \tag{3}$$

where E_{eff_i} is the effective volume energy density of layer i and the gradient is taken with respect to the components of the unit vector $\boldsymbol{u}_i = \boldsymbol{M}_i/M_i$. Let us define a general form for the magnetic free energy density per unit area of the film, E, that may be applied to all the samples considered in this paper. We write

$$\begin{aligned} E = \sum_{i=1,2} d_i \{ &-\boldsymbol{M}_i \cdot \boldsymbol{H} - K_{2i}(\boldsymbol{u}_i \cdot \boldsymbol{k}_i)^2 \\ &+ K_{4i}[(\boldsymbol{u}_i \cdot \boldsymbol{k}_{4xi})^4 + (\boldsymbol{u}_i \cdot \boldsymbol{k}_{4yi})^4] \\ &- M_i(\boldsymbol{u}_i \cdot \boldsymbol{b}_i)H_{ei} + 2\pi M_i^2 u_{iz}^2 \} + A_{12}\boldsymbol{u}_1 \cdot \boldsymbol{u}_2, \end{aligned} \tag{4}$$

where, d_i, K_{2i}, K_{4i}, and H_{ei} are the thickness, uniaxial anisotropy constant, four-fold anisotropy constant and exchange bias field of each layer. In layer i the unit vectors u_i, k_{2i}, k_{4xi}, k_{4yi} and b_i lie parallel to the magnetization, the uniaxial anisotropy axis, the mutually perpendicular four-fold in-plane hard axes, and the exchange bias field, respectively. The constant A_{12} determines the strength of the interlayer coupling. In general the static magnetization in each layer need not lie parallel to the direction of the applied field. Therefore the static magnetization configuration is first obtained by minimizing equation (4) using a steepest descents method. Equation (2) may then be solved for small deviations from the static equilibrium yielding the mode frequencies

$$\omega^2 = \tfrac{1}{2}[(F_1 G_1 + F_2 G_2 + B_1 C_2 + B_2 C_1)$$
$$\pm [(F_1 G_1 + F_2 G_2 + B_1 C_2 + B_2 C_1)^2$$
$$+ 4(G_1 G_2 - B_1 B_2)(C_1 C_2 - F_1 F_2)]^{1/2}], \quad (5)$$

in which

$$F_i = \gamma_i \left[H \cos \phi_i + H_{ei} \cos(\phi_i - \phi_{ei}) + \frac{2K_{2i}}{M_i} \cos 2(\phi_i - \phi_{2i}) \right.$$
$$\left. - \frac{4K_{4i}}{M_i} \cos 4(\phi - \phi_{4i}) - \frac{A_{12}}{M_i d_i} \cos(\phi_1 - \phi_2) \right], \quad (6)$$

$$G_i = \gamma_i \left[H \cos \phi_i + H_{ei} \cos(\phi_i - \phi_{ei}) + \frac{2K_{2i}}{M_i} \cos^2(\phi_i - \phi_{2i}) \right.$$
$$- \frac{K_{4i}}{M_i} (3 + \cos 4(\phi - \phi_{4i}))$$
$$\left. + 4\pi M_i - \frac{A_{12}}{M_i d_i} \cos(\phi_1 - \phi_2) \right], \quad (7)$$

$$B_i = \frac{\gamma_i A_{12}}{M_i d_i}, \qquad C_i = B_i \cos(\phi_1 - \phi_2). \quad (8)$$

Here ϕ_i, ϕ_{2i} and ϕ_{4i} are the angles that M_i, k_{2i}, and k_{4xi} describe with H. The geometry is shown in figure 3. The angle ϕ_i is either obtained from the calculation of the static configuration or else assumed to be zero when the static field strength is sufficiently large. Equation (5) predicts that two resonant modes will occur. In the absence of interlayer coupling, these are simply the uniform mode solutions for the indivdual layers, given by

$$\omega^2 = \gamma^2 \left[H \cos \phi + H_e \cos(\phi - \phi_e) + \frac{2K_2}{M} \cos 2(\phi - \phi_2) \right.$$
$$\left. - \frac{4K_4}{M} \cos 4(\phi - \phi_4) \right] \times \left[H \cos \phi + H_e \cos(\phi - \phi_e) \right.$$
$$+ \frac{2K_2}{M} \cos^2(\phi - \phi_2)$$
$$\left. - \frac{K_4}{M} (3 + \cos 4(\phi - \phi_4)) + 4\pi M \right]. \quad (9)$$
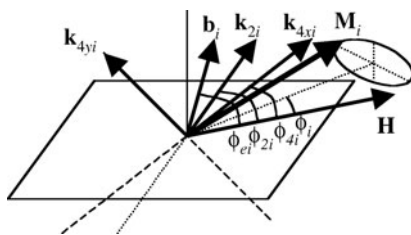
Otherwise they correspond to 'acoustic' and 'optical' modes in which the magnetizations of the two layers precess in and out of phase, respectively. Equations (5)–(9) may be used to simulate the dependence of the observed mode frequencies upon the strength and orientation of the static field, allowing the values of the anisotropy, exchange bias and exchange coupling constants to be deduced.

4. Experimental results

We now illustrate how the measurement technique may be applied to single and multilayered films and micron scale thin film elements.

4.1. A Co thin film

A sample with structure Si(100)/Co(100 Å)/Al$_2$O$_3$(100 Å) was fabricated by magnetron sputtering and positioned under a transmission line structure fabricated on a glass cover slip as shown in figure 2. The transmission line tracks were formed from Al and had width and separation of 30 μm. The probe beam was directed onto the sample at an angle of incidence of 47°, as shown in figure 1, with the plane of incidence parallel to the length of the transmission line. The probe spot was positioned at the centre of the transmission line where the pulsed field lies perpendicular to the plane of the sample. Measurements of dynamic Kerr rotation were then made with the static field applied perpendicular (A) and parallel (B) to the plane of incidence as shown in figure 4. The static magnetic field was set by approaching the desired value from positive saturation.

The dynamic Kerr rotation obtained for various field strengths is shown in figure 5. In general it is necessary to subtract a background from the raw data. This is easily done since no magnetic signal should be obtained at negative time delays. It is usually found that the background is insensitive to the static field strength, suggesting that it is of non-magnetic origin. Non-magnetic contributions to the detector output may arise from pump light scattered into the detector, electrical interference generated by the current in the transmission line, or vibration of the transmission line that leads to a periodic deflection of the probe beam. For a small amplitude precession, the tip of the magnetization vector moves in a plane perpendicular to the initial magnetization direction so that there are only two time dependent components
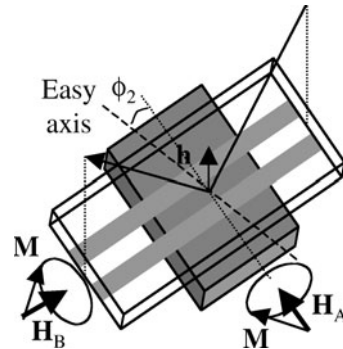

Figure 3. The geometry used for the calculation of the allowed mode frequencies is shown.

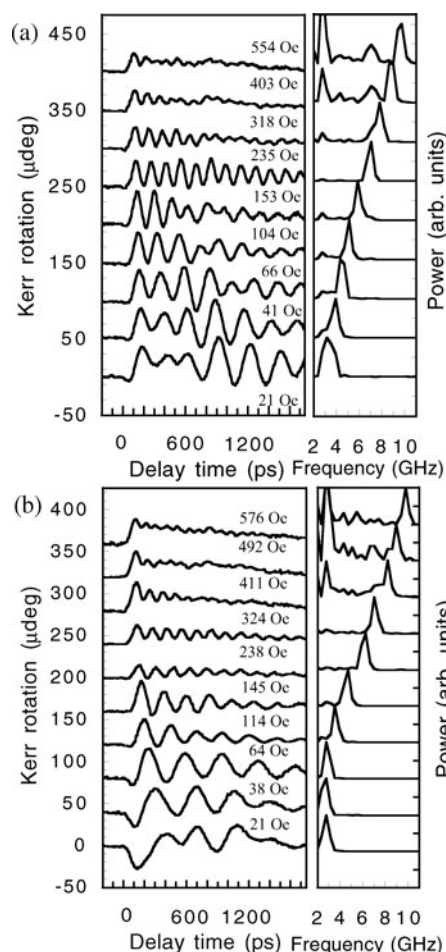**Figure 4.** The measurement geometry used in the study of the single Co film is shown.

Figure 5. The time dependent Kerr rotation data and power spectra obtained from the Co film are shown. The data in panels (*a*) and (*b*) were acquired in the measurement geometries A and B shown in figure 4.

Figure 6. The precession frequencies determined from the power spectra in figure 5 are plotted against the value of the static applied magnetic field. The curves were calculated from equation (9).

of the magnetization. The probe beam senses a mixture of these oscillatory components, as we discuss below, leading to a damped oscillation of the measured Kerr rotation. The frequency of oscillation has a strong dependence on the strength of the static magnetic field as one would expect from equation (9). In some cases we see irregular changes in the amplitude and phase of oscillation. These are caused by secondary peaks in the pulsed field profile that result from reflections of the current pulse within the switch and transmission line. The effect depends upon the precise phase of the secondary peak relative to the magnetization precession and so different behaviour is observed for different static field strengths.

The power spectra of the Kerr rotation scans may be obtained by means of fast Fourier Transforms as shown in figure 5. Clear peaks are observed from which the precession frequency has been determined as the median of the half-height frequencies. The precession frequency has been plotted in figure 6, with error bars that have total length equal to the full width half maximum of the corresponding peaks. The power spectra in figure 5 have been normalized so that the peak height is the same at each field value. However the amplitude of the Kerr rotation decreases as the field is increased and so the normalization process magnifies background peaks
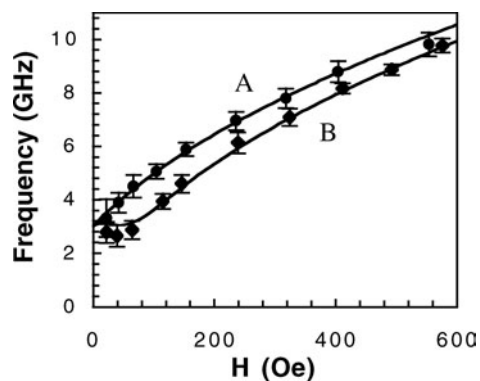
in the higher field scans. We see that there are additional peaks, generally at lower frequency, that are associated with reflections of the current pulse on the transmission line. These peaks may be rejected since their position is independent of the static field strength. Equation (9) was used to simulate the measured frequencies, with the assumption that there is no exchange bias field or four-fold anisotropy present. Assuming the bulk value of $1480 \, \mathrm{emu \, cm^{-3}}$ for the magnetization, best agreement between simulation and data was obtained for a *g* factor of 2.15, a uniaxial anisotropy constant of $4 \times 10^4 \, \mathrm{erg \, cm^{-3}}$, and with the uniaxial easy axis set 20° from the direction of the static field in measurement configuration A. The agreement between measurement and simulation is very good except for the lowest field values in configuration B where the static field is applied close to the in-plane hard axis. This may be because the static and dynamic magnetization are non-uniform in this field regime.

Further information may often be obtained from the detailed form of the Kerr rotation data. However this requires a careful consideration of the optical configuration and a knowledge of the temporal form of the pulsed field. The pulsed field profile can be measured by means of either an electro-optic [30] or magneto-optical sampling technique [31]. The latter exploits the high frequency precession induced in a test sample in the presence of a large static field. In principle we might use the highest field scans obtained from the sample. However in the present case this yields a bandwidth of about 10 GHz that is inadequate to resolve all the important features of the pulsed field. The pulsed field profile may also be obtained by simultaneously fitting the entire set of field scans. This is a tedious process and instead we present a simple illustrative simulation of just one scan, which corresponds to a field value of 235 Oe in figure 5(*a*). The pulsed field is assumed to rise to its maximum value after 100 ps and then relax with a time constant of 1 ns. A value of 0.001 was assumed for the damping constant. The simulation in figure 7(*a*) assumes values of 3.01+4.82i [32] and 0.029 − 0.011i [33] for the refractive index and magneto-optic constant, respectively, while the effect of the Al_2O_3 overlayer is neglected. The deflection of the magnetization from the equilibrium direction, which lies 3.6° from the direction of the static field, is shown in figure 7(*b*). The peak pulsed field at the surface of the transmission line was estimated to be 13 Oe
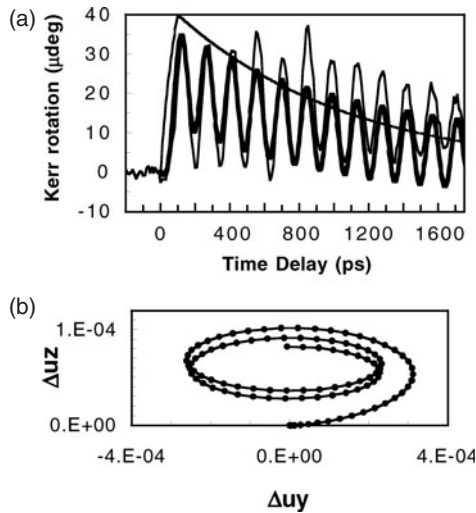
Figure 7. (*a*) The Kerr rotation data obtained in configuration A at an applied field of 235 Oe is plotted (fine curve) with a simulation (bold curve) obtained from a numerical solution of equation (1). The monotonic curve shows the assumed time dependence of the pulsed field. (*b*) The trajectory of the magnetization corresponding to the bold curve in (*a*) is plotted for the first 200 ps. Successive data points are separated by a time interval of 4 ps.

from measurements of the pulsed current, however a peak value of just 1.5 Oe was assumed in the simulations. This suggests that the separation between transmission line and sample was rather large in these particular measurements. The simulation reproduces the phase of the measured oscillations. From figure 7(*b*) it can be seen that the magnetization undergoes a maximum deflection of about 0.02°. From figure 4(*a*) we see that both oscillatory components of the magnetization lie within the plane of incidence and contribute to the Kerr signal through the longitudinal and polar Kerr effects. As the static field is increased the trajectory of the magnetization becomes less elliptical because it is harder to deflect the magnetization within the film plane. The polar Kerr effect is generally an order of magnitude larger than the longitudinal effect and so the out of plane component of magnetization increasingly dominates the Kerr signal as H is increased. It is often possible to deduce the value of the damping constant by comparing the decay of the measured and simulated signals [17]. This cannot be done reliably in the present case due to the secondary peaks in the pulsed field that perturb the decay envelope. It is also important to realize that the observed damping may arise due to a variety of processes, such as generation of eddy currents and spin-wave generation, in addition to the intrinsic mechanism associated with spin–orbit coupling.

4.2. A Co/Cu/Ni$_{81}$Fe$_{19}$/IrMn spin-valve

We next show that the optical FMR technique may be applied to multilayered structures by considering a Si(100)/Ta(50 Å)/ Ni$_{81}$Fe$_{19}$(50 Å) / Cu(20 Å) / Co(50 Å) / IrMn(100 Å) / Ta(30 Å) spin-valve structure prepared by magnetron sputtering. A bias field of about 200 Oe was applied during the growth in order to set the direction of the exchange bias field from the IrMn and the uniaxial anisotropy in the ferromagnetic layers. The sample was again placed underneath a transparent transmission line structure similar to that used in the previous section. The
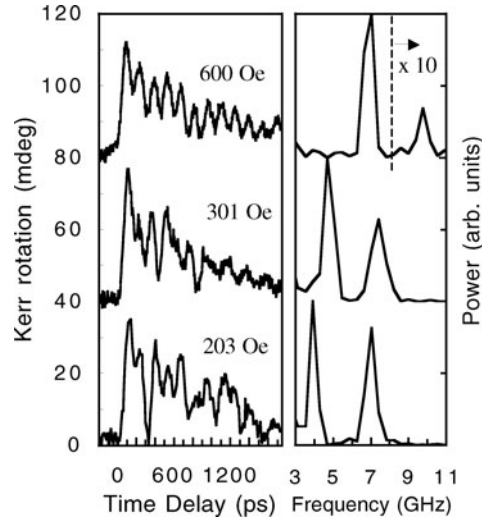

Figure 8. Typical time dependent Kerr rotation data and associated power spectra obtained from the spin-valve sample are shown. The static magnetic field was applied as in configuration A of figure 4. Part of the scan acquired at a field of 600 Oe has been scaled by a factor of 10 in the vertical direction.
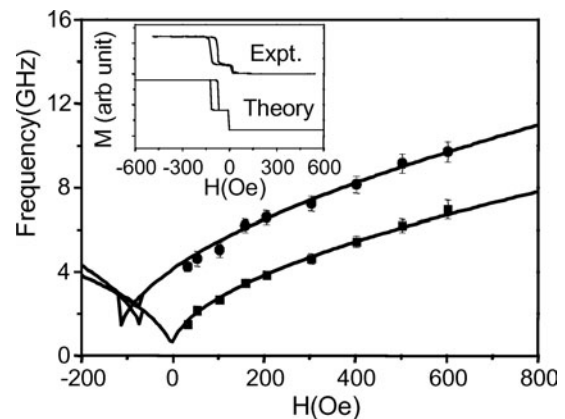

Figure 9. The frequencies of the resonant modes observed in the spin-valve sample are plotted against the value of the static magnetic field. The inset shows MOKE hysteresis loops obtained from the sample.

plane of incidence of the probe lay parallel to the tracks and perpendicular to the sample easy axis. The static magnetic field was applied parallel to the easy axis (configuration A in figure 4) and measurements were made for different values of the static magnetic field strength. Typical scans are shown together with their power spectra in figure 8. The form of the Kerr rotation signal suggests that there may be two or more frequencies beating together. This is confirmed by the power spectra where two field dependent peaks are seen. The intensity of the higher frequency mode decreases as the field is increased as has been observed previously in BLS studies of trilayer structures with ferromagnetic interlayer coupling [34].

The field dependence of the mode frequencies and MOKE hysteresis loops are shown in figure 9. The MOKE loops were acquired with a continuous wave HeNe laser at a wavelength of 633 nm on a different apparatus where it is easier to rotate the sample relative to the plane of incidence. The form of the loop is checked with the Ti : sapphire laser before making a time

dependent measurement. The loops at the shorter wavelength usually display less noise because the saturation Kerr rotation is larger. The loops were modelled by minimizing the free energy in equation (4) while the mode frequencies were simulated from equations (5)–(8). A single set of material parameters was found to reproduce all the experimental data. Values of 2.1 and 2.0 were assumed for the g factors of the Co and $Ni_{81}Fe_{19}$, while values of 14.4 and 9.8 kOe were obtained for the demagnetizing fields, which compare with bulk values of 17.9 kOe and 10 kOe, respectively. The measured and simulated frequencies were found to agree within experimental error as the values of $4\pi M_i$ were adjusted by $\pm 5\%$, so it seems that there is a significant reduction of the Co demagnetizing field which may be associated with either a reduced magnetic moment or the presence of a perpendicular anisotropy. The uniaxial anisotropy field, $2K_2/M$, was found to be equal to 52 Oe for the Co layer, similar to that for the single Co film in the previous section, and to 3 Oe for the $Ni_{81}Fe_{19}$ layer. An exchange bias field of 95 Oe is responsible for shifting both the centre of the minor hysteresis loop associated with the Co, and the minimum in the upper frequency branch, from zero field. We find that there is also a small ferromagnetic coupling, with coupling constant $A_{12} = -0.0015\,erg\,cm^{-2}$, between the two ferromagnetic layers. Further details of the variation of the coupling constant with the thickness of the Cu layer are given in [35].

The calculation of the magneto-optical response of the sample is considerably more complicated in the case of a multilayer both in terms of the calculation of the trajectories of the coupled magnetic moments, and due to the need to consider the interference of the multiply reflected optical field. However this is certainly an important area for future investigation since the damping and switching mode of the $Ni_{81}Fe_{19}$ sense layer is of considerable importance within magnetic recording technology.

4.3. A micron scale $Ni_{81}Fe_{19}$ element

Finally we provide an example of how the optical FMR technique may be applied to micron scale thin film elements. The sample was a square $Ni_{81}Fe_{19}$ element, grown on a glass cover slip, and capped with a 20 nm protective layer of Al_2O_3. The $Ni_{81}Fe_{19}/Al_2O_3$ bilayer was sputtered onto electron beam resist in a magnetic field of 150 Oe. The unwanted material was then removed by a lift-off process. The squares were 10 μm wide and 150 nm thick, with an edge-to-edge separation of 60 μm. Pump probe measurements were made in a different configuration to those described previously. The transmission line structure was fabricated upon a semi-insulating GaAs substrate with the tracks facing upwards. The sample was placed face down on the transmission line and probed through the glass substrate using a cover slip corrected microscope objective (NA = 0.65) to obtain a sub-micron focused spot. The cover slip was positioned so that one of the elements lay in the centre of one of the conducting tracks of the transmission line. One edge of the element lay parallel to the track and hence perpendicular to the in-plane pulsed field. The full area of the back-reflected probe beam was directed into the detector in order to sense the out of plane component of the dynamic magnetization.

Measurements were first made with the probe spot focused at the centre of the element. Typical scans are shown in figure 10 with the static field applied parallel to an edge of the square. While clear oscillations are observed for a static field of 288 Oe, they become much more irregular when the field is reduced to 76 Oe. Measurements were made with a constant static field applied in different directions within the plane of the sample. The Fourier power spectra revealed a single resonance and the dependence of the frequency upon the orientation of the static field has been plotted in figure 11 for two field values. The frequency oscillates with a period of 90°, suggesting that the anisotropy is predominantly four-fold. The frequency maxima and minima occur when the field is applied parallel to the edge and diagonal, respectively. However there is also a slower underlying variation with a period of 360° that results from the presence of the in-plane pulsed field. The curves in figure 11 were calculated from equation (9) in the absence of an exchange bias field, but with the term $H\cos\phi$ modified by the addition of a term $h\cos(\phi - \phi_h)$ in which h is the time-averaged pulsed field and ϕ_h is the
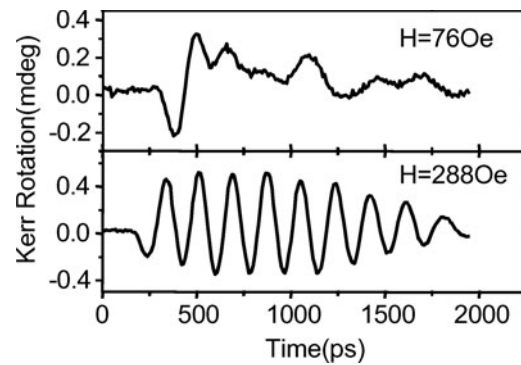

Figure 10. The time dependence of the polar Kerr rotation at the centre of the square element is shown. The static magnetic field was applied parallel to one of the edges of the square.
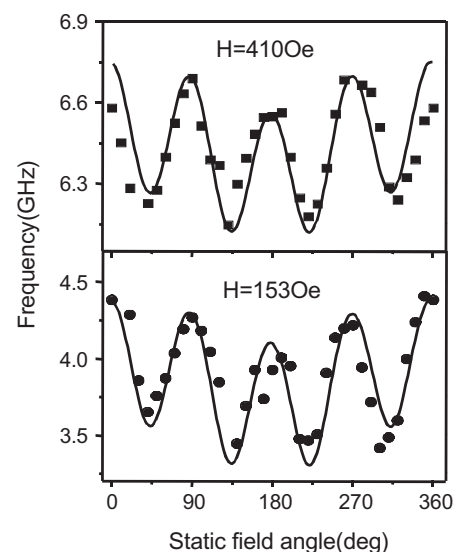

Figure 11. The dependence of the precession frequency at the centre of the square element upon the orientation of the static field within the plane of the sample is shown. At 0° the static field lies parallel to the in-plane pulsed field.

angle between the pulsed field h and the static field H. While measurements of the current amplitude suggested a peak value of 27 Oe for the pulsed field, a value of 12 Oe was assumed for the curves in figure 11. The time averaged pulsed field is expected to be about half the peak value, so this suggests that close contact was achieved between the sample surface and the transmission line. The curves also assume values of 2.1 for the g factor and 10.8 kOe for the demagnetizing field. The uniaxial anisotropy field, $2K_2/M$, was equal to 2 Oe while the four-fold anisotropy field, $4K_4/M$, was equal to -33 Oe. The uniaxial easy axis was parallel to the edge along which the magnetic field was applied during the sample growth. The four-fold easy axes were parallel to the edges of the square. The four-fold anisotropy is associated with non-uniformity of the static magnetization within the square element. The apparent size of this anisotropy will depend upon the strength of the applied field, although there was no noticeable variation within the applied field range of 100–600 Oe for which measurements were made.

It was not possible to make a reliable determination of the resonance frequency for applied fields less than about 100 Oe due to the irregular nature of the Kerr signal. Series of dynamic images were acquired for two different values of the static field in order to further investigate this behaviour. Examples are presented in figure 12 where the pixel size in each scan is $0.5 \, \mu$m. The images are slightly distorted (the corners should have an interior angle of 90°) due to a small misalignment but this does not obscure the magnetization dynamics. The grey scale represents the instantaneous value of the out of plane component of the precessing magnetization, so that black and white correspond to the magnetization tilting in and out of plane. The signal has been scaled by the same factor in all images so as to accentuate the contrast while allowing direct comparison of the response at different time delays. For the measurements made with a static field of 288 Oe the precession is initially uniform with non-uniformity developing from the edges as seen in the image at 170 ps. At later times a regular pattern of stripes forms with an anti-node at the centre of the element. The envelope of the oscillations shown in the lower panel in figure 10 is suggestive of beating between two or more modes of slightly different frequency. Unfortunately the length of our translation stage prevents us from making measurements at longer time delays and Fourier transforms of the present data have insufficient resolution to reveal more than a single mode.

For measurements made with a static field of 76 Oe, the precession is non-uniform from the beginning. The image at 100 ps suggests that a domain structure is present before the pulsed field is applied. The magnetization begins by moving orthogonal to the in-plane pulsed field and the static magnetization. The magnetization may be deflected either in or out of the film plane within the different domains and so a strong contrast is observed within the dynamic image. At time delays of 200 and 950 ps the image shows an increasingly irregular pattern of contrast throughout the entire area of the element which presumably leads to the irregular time scan shown in the upper panel in figure 10 where the probe spot was positioned at the centre of the element.
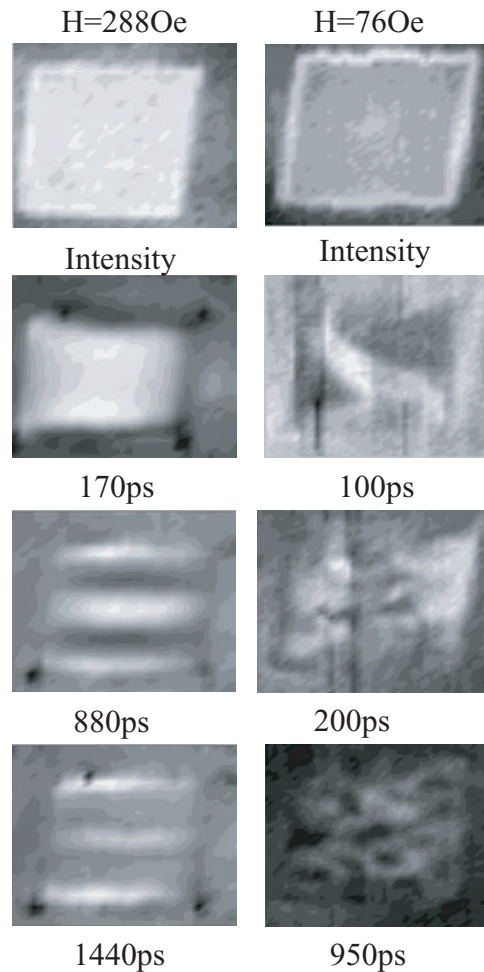
Figure 12. An intensity image and series of time resolved polar Kerr images obtained from the square element are shown for two values of the static field. The static field was applied in the vertical direction and parallel to the uniaxial easy axis of the sample.

5. Discussion

We have shown how the optical FMR technique may be applied to three different types of structure. It is not necessary to deposit the sample onto the transmission line used to deliver the pulsed magnetic field, and measurements can be made on any sample when a transparent transmission line substrate is used. Measurements made upon a continuous 100 Å thick Co film demonstrate that magnetization precession may be clearly observed even when the magnetization is deflected through an angle of less than 20 mdeg. The frequency of precession may therefore be compared with simple formulae obtained by linearizing the Landau–Lifshitz equation of motion. By making measurements with a static magnetic field of varying strength applied in different directions within the plane of the film we have shown that information may be obtained about the g factor, and the anisotropy and demagnetizing fields. The shape of the magnetization trajectory may in principle be deduced through simulation of the Kerr signal. However, this is presently hindered by the fact that the magneto-optical constants are not particularly well known and by the complexity of the optical calculation in anything other than a semi-infinite structure. The damping of the precession

may often be quantified although this proved difficult in this particular instance due to the presence of secondary peaks in the temporal profile of the pulsed field.

The measurements presented from the spin-valve sample demonstrate the feasibility of studying collective excitations in multi-layered structures. Determination of mode frequencies is again relatively straightforward and enables interactions such as exchange bias and interlayer coupling to be quantified. It is useful to perform pump-probe measurements in conjunction with MOKE magnetometry. In principle both measurements may be made with the same apparatus so that the same position on the sample is probed in each case. The dynamic Kerr data also contains information about the relative phase of the magnetization precession in the Co and $Ni_{81}Fe_{19}$ layers. Although this will undoubtedly be important in understanding the reorientation of the $Ni_{81}Fe_{19}$ sense layer in a spin-valve sensor, further work is required in order to reliably interpret the measured magneto-optical response. The precession frequency at the centre of the square $Ni_{81}Fe_{19}$ element was treated with a coherent precession model in order to quantify a four-fold anisotropy related to the shape of the element. However, the images obtained from the square $Ni_{81}Fe_{19}$ element reveal a precession that is inherently non-uniform, even when the static applied field significantly exceeds the anisotropy field, thus challenging the validity of the coherent precession model. The observed stripe pattern suggests the presence of modes with in-plane wave vector. These are most likely magnetostatic volume modes [36] since the wave vector appears to lie parallel to the static field. Further measurements of the precession frequency at points other than the centre of the element are required in order to fully explore the mode spectrum within the sample. It would also be interesting to explore whether similar behaviour is observed in ultrathin elements where the dispersion characteristics of the magnetostatic waves are different. Finally the dynamic images suggest that the non-uniformity of the precession may affect the apparent damping deduced from time scans [23]. Indeed the images are necessary to separate intrinsic damping due to the spin–orbit interaction from dephasing of finite wave vector magnetostatic waves.

6. Outlook

Although the optical pump-probe technique is already a powerful tool for the study of thin film magnetism, there are many opportunities to further extend its application. This paper has been concerned with small perturbations of the magnetization. The generation of larger pulsed fields allows the investigation of non-linear processes, including magnetization reversal. The amplitude of the pulsed field is proportional to the applied voltage bias and the reciprocal of the linear dimension of the transmission line. Fields of order 1 kOe have been obtained when the dimensions of the transmission line have been made sufficiently small [31]. Although only a small sample area can be excited, this approach will be of increasing interest for the study of nanostructures, and may be advantageous when studying the propagation of a magnetic disturbance through a larger structure. The pulse shape may be tailored through the use of multiple photoconductive switches [37]. It will also be necessary to improve the spatial resolution

of the probe channel if nanostructures are to be studied and if the full richness of time dependent micromagnetic processes is to be accessed. Measurements have already been made with a solid immersion lens [38], and there are opportunities to exploit other near field measurement techniques.

It is often complicated to untangle the contributions that different components of the vector magnetization make to the total Kerr signal. However quadrant photodiodes have previously been used to simultaneously detect the longitudinal Kerr signal from the in-plane magnetization components and the polar Kerr signal from the out of plane component [39]. The first use of this arrangement for time dependent measurements was reported recently [40]. Alternatively a combination of transverse and polar Kerr effects [15] or a combination of linear MOKE and MSHG [25] may also be used to measure all three components of the magnetization. The three-dimensional trajectory of the vector magnetization may be plotted if the signal from the different magnetization components can be calibrated.

It has been shown that Fourier transforms of the time dependent Kerr signal can yield the frequencies of excitations present at a specific point in a sample. In a similar way spatial transforms of images should yield information about the corresponding wave vectors of those excitations. It may be necessary to acquire a spatial image at every point in a time scan for the full character of the excitation spectrum to be explored. With the single channel detection schemes currently in use, this is likely to be highly time consuming and so the development of a multiple channel detection scheme is highly desirable.

Finally we note that numerical micromagnetic simulations have advanced rapidly in recent years so that it is possible to directly simulate the dynamic images obtained from pump-probe measurements. We believe that this combination of measurement and modelling tools is likely to find widespread application in the coming years and will prove to be a powerful tool in the development of magnetic nanotechnology.

Acknowledgments

References

[1] 1995 *Ultrathin Magnetic Structures II* chapter 3, ed J A C Bland and B Heinrich (Berlin: Springer)

[2] Baumberg J J, Awschalom D D and Samarth N 1994 *J. Appl. Phys.* **75** 6199

[3] Vaterlaus A, Buetler T and Meier F 1992 *Phys. Rev. Lett.* **46** 5280

[4] Beaurepaire E, Merle J-C, Daunois A and Bigot J-Y 1996 *Phys. Rev. Lett.* **76** 4250

[5] van Kampen M, Jozsa C, Kohlepp J T, LeClair P, Lagae L, de Jonge W J M and Koopmans B 2002 *Phys. Rev. Lett.* **88** 227201

[6] Zhang Q, Nurmikko A V, Anguelouch A, Xiao G and Gupta A 2002 *Phys. Rev. Lett.* **89** 177402

[7] Ju G, Nurmikko A V, Farrow R F C, Marks R F, Carey M J and Gurney B A 1999 *Phys. Rev. Lett.* **82** 3705

[8] Freeman M R, Ruf R R and Gambino R J 1991 *IEEE Trans. Magn.* **27** 4840

[9] Engebretson D M, Berezovsky J, Park J P, Chen L C, Palmstrom C J and Crowell P A 2002 *J. Appl. Phys.* **91** 8040

[10] Crawford T M, Silva T J, Teplin C W and Rogers C T 1999 *Appl. Phys. Lett.* **74** 3386

[11] Metzger G, Pluvinage P and Tourget R 1965 *Ann. Phys.* **10** 5

[12] Freeman M R, Awschalom D D, Hong J M and Chang L L 1990 *Phys. Rev. Lett.* **64** 2430

[13] Aeschlimann M, Bauer M, Pawlik S, Weber W, Burgermeister R, Oberli D and Siegmann H C 1997 *Phys. Rev. Lett.* **79** 5159

[14] Wu J, Moore J R and Hicken R J 2000 *J. Magn. Magn. Mater.* **222** 189

[15] Acremann Y, Back C H, Buess M, Portmann O, Vaterlaus A, Pescia D and Melchior H 2000 *Science* **290** 492

[16] Hiebert W K, Stankiewicz A and Freeman M R 1997 *Phys. Rev. Lett.* **79** 1134

[17] Wu J, Hughes N D, Moore J R and Hicken R J 2002 *J. Magn. Magn. Mater.* **241** 96

[18] Crawford T M, Kabos P and Silva T J 2000 *Appl. Phys. Lett.* **76** 2113

[19] Bauer M, Lopusnik R, Fassbender J and Hillebrands B 2000 *Appl. Phys. Lett.* **76** 2758

[20] Acremann Y, Kashuba A, Buess M, Pescia D and Back C H 2002 *J. Magn. Magn. Mater.* **239** 346

[21] Hiebert W K, Ballentine G E and Freeman M R 2002 *Phys. Rev. B* **65** 140404

[22] Park J P, Eames P, Engebretson D M, Berezovsky J and Crowell P A 2002 *Phys. Rev. Lett.* **89** 277201

[23] Barman A, Kruglyak V V, Hicken R J, Kundrotaite A and Rahman M 2003 *Appl. Phys. Lett.* **82** 3065

[24] Choi B C, Belov M, Hiebert W K, Ballentine G E and Freeman M R 2001 *Phys. Rev. Lett.* **86** 728

[25] Gerrits Th, van den Berg H A M, Hohlfeld J, Bar L and Rasing Th 2002 *Nature* **418** 509

[26] Wu J, Schmool D S, Hughes N D, Moore J R and Hicken R J 2002 *J. Appl. Phys.* **91** 278

[27] Hicken R J, Hughes N D, Moore J R, Schmool D S, Wilks R and Wu J 2002 *J. Magn. Magn. Mater.* **242–245** 559

[28] Patton C E 1984 *Phys. Rep.* **103** 251

[29] Gillete P R and Oshima K 1958 *J. Appl. Phys.* **29** 529

[30] Keil U D, Gerritsen H J, Haverkort J E M and Wolter J H 1995 *Appl. Phys. Lett.* **66** 1629

[31] Elezzabi A Y and Freeman M R 1996 *Appl. Phys. Lett.* **68** 3546

[32] Lide D R (ed) 1994 *Handbook of Chemistry and Physics* 75th edn (Boca Raton: Chemical Rubber)

[33] Krinchik G S and Artem'ev V A 1968 *Sov. Phys. JETP* **26** 1080

[34] Hicken R J, Ives A J R, Eley D E P, Daboo C, Bland J A C, Childress J R and Schuhl A 1994 *Phys. Rev. B* **50** 6143

[35] Barman A, Kruglyak V V, Hicken R J, Marrows C H, Ali M, Hindmarch A T and Hickey B J 2002 *Appl. Phys. Lett.* **81** 1468

[36] Damon R W and Eshbach J R 1961 *J. Phys. Chem. Solids* **19** 308

[37] Gerrits Th, Hohlfeld J, Gielkens O, Veenstra K J, Bal K, Rasing Th and van den Berg H A M 2001 *J. Appl. Phys.* **89** 7648

[38] Freeman M R, Elezzabi A Y and Stotz J A H 1997 *J. Appl. Phys.* **81** 4516

[39] Wright C D, Clegg W W, Boudjelmine A and Heyes N A E 1994 *Japan. J. Appl. Phys.* **33** 2058

[40] Hiebert W K, Ballentine G E, Lagae L, Hunt R W and Freeman M R 2002 *J. Appl. Phys.* **92** 392